nature energy

Article

https://doi.org/10.1038/s41560-023-01262-3

Solar-driven liquid multi-carbon fuel production using a standalone perovskite–$BiVO_4$ artificial leaf

Received: 22 July 2022

Accepted: 14 April 2023

Published online: 18 May 2023

Check for updates

Motiar Rahaman[1], Virgil Andrei[1], Demelza Wright[2], Erwin Lam[1], Chanon Pornrungroj[1], Subhajit Bhattacharjee[1], Christian M. Pichler[1], Heather F. Greer[1], Jeremy J. Baumberg[2] & Erwin Reisner[1]

The synthesis of high-energy-density liquid fuels from CO_2 and H_2O powered by sunlight has the potential to create a circular economy. Despite the progress in producing simple gaseous products, the construction of unassisted photoelectrochemical devices for liquid multi-carbon production remains a major challenge. Here we assembled artificial leaf devices by integrating an oxide-derived $Cu_{94}Pd_6$ electrocatalyst with perovskite–$BiVO_4$ tandem light absorbers that couple CO_2 reduction with water oxidation. The wired $Cu_{94}Pd_6$|perovskite–$BiVO_4$ tandem device provides a Faradaic efficiency of ~7.5% for multi-carbon alcohols (~1:1 ethanol and *n*-propanol), whereas the wireless standalone device produces ~1 μmol cm^{-2} alcohols after 20 h unassisted operation under air mass 1.5 G irradiation with a rate of ~40 μmol h^{-1} $g_{Cu94Pd6}{}^{-1}$. This study demonstrates the direct production of multi-carbon liquid fuels from CO_2 over an artificial leaf and, therefore, brings us a step closer to using sunlight to generate value-added complex products.

Approaches for the sunlight-driven conversion of the greenhouse gas CO_2 into fuels are often animated by a bio-inspired process known as 'artificial photosynthesis', where solar energy is stored in the products as chemical energy[1,2]. High-energy-density oxygenates such as multi-carbon alcohols are particularly attractive products as they can be easily stored, transported and directly used as liquid fuels[3,4]. Although the electrochemical conversion of CO_2 to multi-carbon alcohols is being explored[5–8], direct solar-driven alcohol production from aqueous CO_2 over an artificial leaf has yet to be demonstrated to sustainably produce multi-carbon liquid fuels.

Lead halide perovskites have been established in recent years among the most promising light absorbers in photovoltaic electricity generation[9–12] and in solar-driven catalytic processes[13–15]. The perovskite light absorbers can either be used in an indirect configuration to provide bias voltage in photovoltaics coupled to electrolysis systems[16–18] or for direct solar-to-chemical conversion immersed in solution when encapsulated and coupled to a catalyst in an integrated photoelectrochemical (PEC) device[19–21]. The combination of a perovskite-based photocathode and a water-oxidizing $BiVO_4$ photoanode was previously employed as a tandem platform for the reduction of CO_2 to syngas (gas mixture containing CO and H_2) or selective CO formation with a molecular or metal alloy catalyst, respectively[22,23]. However, C–C bond formation to generate multi-carbons has not yet been achieved with these tandem devices under bias-free conditions. Multi-carbon hydrocarbons and oxygenates have been generated with moderate efficiency using indirect photovoltaics coupled to electrolysis systems, where commercially available solar cells were externally employed to generate sufficient voltage for product formation[24,25] or using a Si-based photocathode under additional electrical bias[26].

Formation of multi-carbon products from CO_2 and H_2O over conventional Cu catalysts requires large overpotentials (<−0.8 V versus the reversible hydrogen electrode (RHE))[27,28]. Established tandem

[1]Yusuf Hamied Department of Chemistry, University of Cambridge, Cambridge, UK. [2]NanoPhotonics Centre, Cavendish Laboratory, Department of Physics, University of Cambridge, Cambridge, UK. e-mail: reisner@ch.cam.ac.uk

https://doi.org/10.1038/s41560-023-01262-3

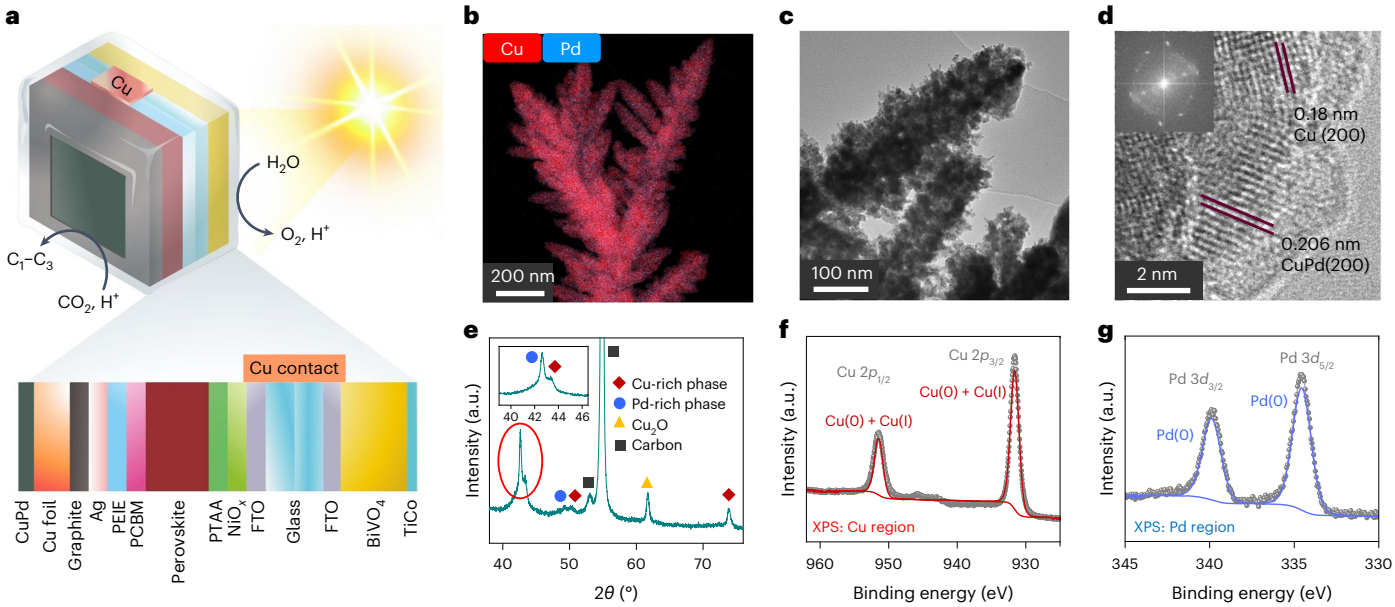

Fig. 1 | Artificial leaf overview and physical characterization of the bimetallic catalyst. a, Schematic representation of a wireless standalone $BiVO_4$–perovskite|$Cu_{94}Pd_6$ artificial leaf. **b**–**g**, The oxide-derived $Cu_{94}Pd_6$ catalyst was characterized by STEM-EDX mapping (**b**), TEM (**c**), HR-TEM (**d**), powder XRD analysis (**e**; inset: expansion of area under the red oval), and XPS analysis for Cu (**f**) and Pd (**g**) regions (grey dots indicate data points; coloured lines indicate fits).

PEC devices therefore do not provide sufficient bias for unassisted multi-carbon generation and limit product formation only to C_1 products[22,23,29]. Hence, there remains a challenge to assemble an integrated standalone PEC platform that allows for unassisted production of multi-carbon (C_{2+}) fuels from CO_2 and water using sunlight. To overcome this challenge, improvements on both catalyst and light absorber sides are required.

In this study, a bimetallic $Cu_{94}Pd_6$ electrocatalyst has been employed that can produce multi-carbon alcohols from CO_2 at low overpotentials. The perovskite architecture has been modified with an additional poly(bis(4-phenyl)(2,4,6-trimethylphenyl)amine) (PTAA) hole transport layer to improve the open-circuit voltage (V_{oc}) to increase the available bias for catalysis. The $Cu_{94}Pd_6$ catalyst has been successfully integrated in a bias-free, wired perovskite–$BiVO_4$ tandem device and a wireless standalone artificial leaf configuration for unassisted multi-carbon alcohol production from aqueous CO_2 powered by simulated sunlight.

Preparation and characterization of the bimetallic catalyst

Cu is the only known metal that can form multi-carbon products from CO_2 electroreduction but requires relatively large overpotentials and suffers from low product selectivity[27,30,31]. The product selectivity can be tuned by doping a second metal to copper, and generally, a CO-forming metal (such as Ag, Pd) can improve the multi-carbon product efficiency during CO_2 reduction[32–36]. Following a reported protocol[36], we have therefore prepared an oxide-derived Cu_xPd_y material for multi-carbon alcohol production from CO_2 and H_2O at low overpotentials to improve energy efficiency and enable bias-free operation with our perovskite–$BiVO_4$ artificial leaf configuration (Fig. 1a). A template-assisted electrodeposition method was employed to form a dendritic macroporous structure of the bimetallic Cu_xPd_y catalyst (Supplementary Fig. 1). To promote multi-carbon production at low overpotentials, the as-prepared Cu_xPd_y material was then further activated by a three-step activation process. First, the material was anodized in a basic ethylene glycol–water mixture to form a rough oxide layer. Then, the anodized material was further annealed in air to extend the bulk oxide phase. Finally, the thick oxide layer was electrochemically reduced to form an oxide-derived bimetallic material (Supplementary Fig. 1), which is the active catalyst (Methods).

The metal composition of the activated bimetallic catalyst was determined by inductively coupled plasma optical emission spectrometry (ICP-OES) analysis, showing a Cu:Pd ratio of 94:6 (thus the material is referred to as $Cu_{94}Pd_6$, Supplementary Fig. 2). ICP-OES results also show that the elemental distribution of the $Cu_{94}Pd_6$ catalyst is almost unchanged after the activation. Scanning electron microscopy (SEM) analysis reveals the macroporous structure of the as-prepared catalyst, and the macroporous morphology remains unchanged after activation (Supplementary Fig. 3). The average surface pore size of the catalyst is 30 ± 4 μm. Cross-sectional SEM analysis reveals a catalyst layer thickness of 85 ± 5 μm (Supplementary Fig. 4). Transmission electron microscopy (TEM) analysis reveals that the pore side walls consist of dendritic structures (Supplementary Fig. 5). The high-angle annular dark-field scanning transmission electron microscopy energy dispersive X-ray spectroscopy (HAADF-STEM-EDX) mapping of the activated $Cu_{94}Pd_6$ catalyst shows a phase separation where a Cu-rich phase ($Cu_{99}Pd_1$) and a Pd-rich phase ($Cu_{85}Pd_{15}$) are present on the dendrites (Fig. 1b and Supplementary Fig. 6). Phase separation is introduced by the activation process as the as-prepared catalyst shows a homogeneous distribution of Cu and Pd on the surface with a 94:6 metal ratio (Supplementary Fig. 6).

TEM analysis further reveals the presence of nanocrystals on the dendritic surface of the activated $Cu_{94}Pd_6$ catalyst that provide a high electrochemically active surface area (Fig. 1c and Supplementary Fig. 7). High-resolution TEM (HR-TEM) analysis provides the fringe patterns showing the presence of the Cu(200) and CuPd(200) planes on the surface (Fig. 1d). The fast-Fourier transform (FFT) pattern of the activated $Cu_{94}Pd_6$ material shows a polycrystalline lattice system (inset Fig. 1d). Powder X-ray diffraction (XRD) analysis of the as-prepared $Cu_{94}Pd_6$ catalyst shows CuPd alloy peaks (Supplementary Fig. 8) and phase separation after activation is confirmed by the presence of separate Cu-rich and Pd-rich phases (Fig. 1e; the C peaks at $2\theta \approx 53°$ and 55° come from the graphite foil substrate). X-ray photoelectron spectroscopy (XPS) shows only the presence of Cu (Cu $2p_{1/2}$, Cu $2p_{3/2}$ peaks) and Pd (Pd $3d_{3/2}$, Pd $3d_{5/2}$ peaks) on the surface of the material with no other heavy metal (for example, Pt) contamination (Fig. 1f,g

https://doi.org/10.1038/s41560-023-01262-3

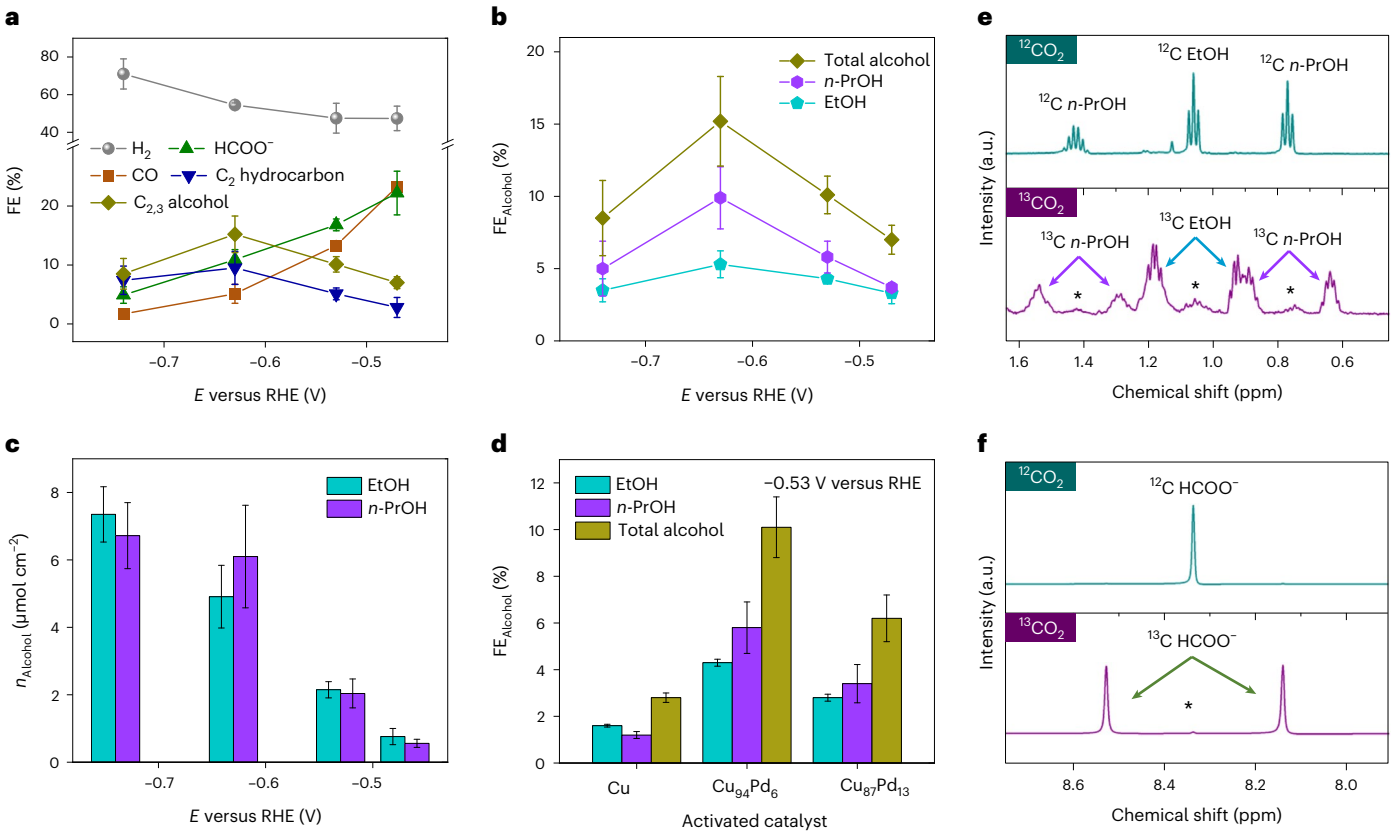

Fig. 2 | Electrochemical analysis of activated Cu_xPd_y catalysts. a, FE of H_2 and C_1–C_3 products from the potential-dependent CO_2 electrolysis experiments over the activated $Cu_{94}Pd_6$ catalyst. *E*, applied potential. The *y*-axis break helps to show the product distribution more clearly. **b**,**c**, FE (**b**) and corresponding amounts of individual alcohol ($n_{Alcohol}$) products (**c**) from controlled-potential electrolysis experiments (formation of ethanol (EtOH) and *n*-propanol (*n*-PrOH) requires 12 e^- and 18 e^- transfers, respectively). **d**, Composition-dependent activity of different activated Cu_xPd_y systems. CO_2-saturated 0.5 M $KHCO_3$ (pH 7.2) was used as electrolyte, and the experiments were performed for 4 h. **e**,**f**, Isotopic labelling experiments were carried out at −0.53 V versus RHE for 12 h using $^{12}CO_2$-saturated and $^{13}CO_2$-saturated 0.5 M KOH electrolyte (pH 7.3) to demonstrate by ^{1}H NMR spectroscopy that the multi-carbon alcohols (**e**) and formate (**f**) were produced from CO_2. The asterisks in **e** and **f** denote trace amounts of unlabelled products from other carbon sources (for example, some natural abundance of $^{12}CO_2$ in the $^{13}CO_2$ cylinder). All experiments were carried out at room temperature. The mean values were estimated from three independent ($n = 3$) measurements, and the data are presented as mean values ± s.d.

and Supplementary Fig. 9). It is noted that Cu(0) and Cu(I) species for the Cu 2*p* peaks appear at similar binding energy and are thus difficult to distinguish by XPS. A Cu(I) species can be formed by aerial surface oxidation but would instantaneously be reduced back to the metallic phase under CO_2 reduction conditions.

Electrocatalytic CO_2 reduction

The activated $Cu_{94}Pd_6$ catalyst was electrochemically studied in CO_2-saturated aqueous 0.5 M $KHCO_3$ buffer electrolyte (pH 7.2) at room temperature using a two-compartment cell separated by a proton exchange membrane (Nafion[117]). A three-electrode set-up was employed where the activated $Cu_{94}Pd_6$ catalyst was used as a working electrode, a Pt mesh as a counter electrode and a Ag/AgCl electrode (saturated NaCl) as a reference electrode. Cyclic voltammetry (CV) analysis provides an indication of the low overpotential activity of the activated $Cu_{94}Pd_6$ catalyst (Supplementary Fig. 10). Controlled potential electrolysis (CPE) was carried out for 4 h to show the potential dependent product distribution over the oxide-derived phase-separated $Cu_{94}Pd_6$ catalyst in a potential window from −0.47 V to −0.74 V versus RHE (Fig. 2a). Multi-carbon alcohol formation gradually increases when applying a more negative potential; starting at −0.47 V versus RHE with a Faradaic efficiency (FE) of (7.0 ± 1.0)% and reached a maximum FE of (15.2 ± 3.1)% at −0.63 V versus RHE (Fig. 2b). The alcohol consisted of ethanol and *n*-propanol with a propanol to ethanol FE ratio of ~2:1 at −0.63 V versus RHE. The total amount of alcohol also gradually increased with applied potential, with 6.1 ± 1.5 μmol cm^{-2} *n*-propanol and 4.91 ± 0.93 μmol cm^{-2} ethanol being produced at −0.63 V versus RHE (Fig. 2c).

Activation is essential for the performance of the bimetallic catalyst (Supplementary Fig. 11); at −0.53 V versus RHE, the as-prepared $Cu_{94}Pd_6$ alloy catalyst showed (0.4 ± 0.1)% total alcohol FE, whereas the activated, phase-separated catalyst formed (10.1 ± 1.3)% multi-carbon alcohols. Furthermore, the typical active potential range for multi-carbon alcohol formation on a copper surface is −0.85 V to −1.1 V versus RHE[5,27,30], whereas the phase-separated bimetallic catalyst already displayed maximum alcohol efficacy at −0.63 V versus RHE. Therefore, the activated bimetallic system works efficiently at ≥250 mV more positive potential and is thus suitable for unassisted PEC devices. The effect of element composition in the bimetallic catalyst was studied in CPE experiments at −0.53 V versus RHE with activated Cu, $Cu_{94}Pd_6$ and $Cu_{87}Pd_{13}$ catalysts. Maximum efficiency was obtained on activated $Cu_{94}Pd_6$ catalyst where ~10.1% alcohols were formed (Fig. 2d). Both oxide-derived pure Cu and higher Pd-content catalyst $Cu_{87}Pd_{13}$ show a low yield towards alcohol formation from aqueous CO_2 due to the inadequate surface composition (homogeneously distributed Cu-rich and Pd-rich phases; Supplementary Fig. 12), indicating oxide-derived $Cu_{94}Pd_6$ as the optimum material. Isotopic labelling experiments using $^{13}CO_2$ were carried out, performing CPE at an applied potential of −0.53 V versus RHE for 12 h, and ^{1}H nuclear magnetic resonance

https://doi.org/10.1038/s41560-023-01262-3

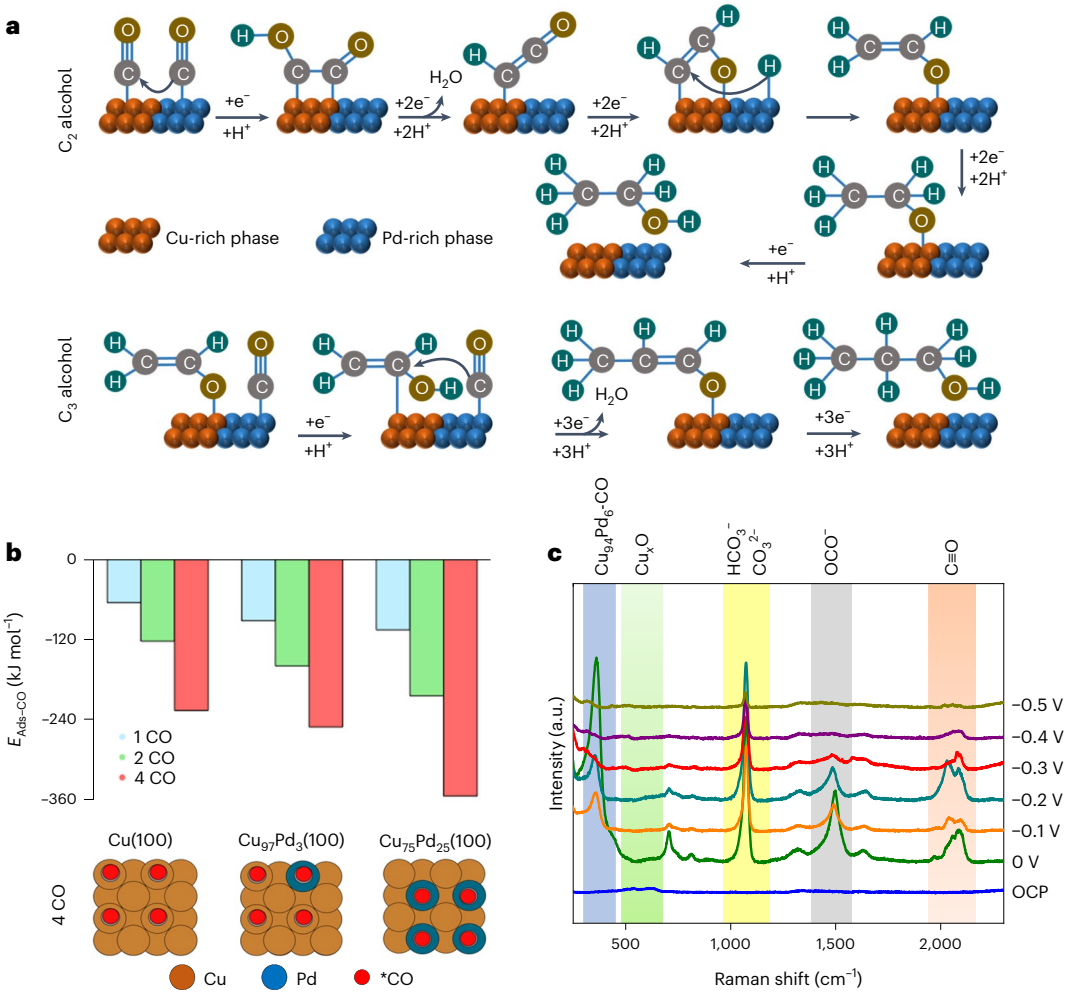

Fig. 3 | Mechanistic analysis of multi-carbon production over activated $Cu_{94}Pd_6$ catalyst at low overpotentials. a, Proposed mechanism of multi-carbon alcohol formation over a phase-separated CuPd system (based on refs. 36,40). The initial CO_2 to *CO reduction step is not shown; it occurs through a conventional pathway involving $2e^-$ (ref. 40). **b**, DFT study shows preferred *CO adsorption on a Cu_xPd_y system compared to pure metallic Cu. E_{Ads-CO}, *CO adsorption energy. **c**, Operando Raman spectroscopy study with the activated $Cu_{94}Pd_6$ catalyst shows strong *CO adsorption at very low overpotentials, which may explain the catalyst's multi-carbon-generating activity. The coloured vertical shaded bars highlight different Raman features. OCP, open circuit potential. The applied potential values are versus RHE scale.

(^{1}H NMR) analysis confirmed that the products were formed solely from CO_2 as the expected peak splitting (J_{C-H} coupling) was observed under a $^{13}CO_2$ atmosphere (Fig. 2e,f). The bicarbonate electrolyte (pH 7.3) for the isotopic labelling experiments was prepared by saturating $^{12}CO_2$ or $^{13}CO_2$ into 0.5 M 99.999% KOH solution.

Density functional theory and operando Raman spectroscopy studies

The formation of multi-carbon alcohols on the activated $Cu_{94}Pd_6$ catalyst likely occurs through a synergistic process involving both the Cu-rich and the Pd-rich phases. The mechanism of multi-carbon product formation on the phase-separated $Cu_{94}Pd_6$ catalyst can be explained by *CO and *H spillover (* represents an adsorption site) from the Pd-rich to the Cu-rich phase, where C–C coupling is followed by hydrogenation[36,37]. Pd is known as a CO-forming catalyst in electrochemical CO_2 reduction, and the high abundance of *CO on the Pd-rich phase[38] accelerates *CO dimerization through spillover to *CO at the Cu-rich phase to form multi-carbon products. After dimerization, the C_2 intermediate is reduced (via hydrogenation) to form ethanol as a product, or another *CO can be added to the C_2 intermediate forming a C_3 oxygenate intermediate, which is then reduced to *n*-propanol[39,40]. Figure 3a shows a proposed schematic representation of the multi-carbon forming mechanism on the phase-separated bimetallic catalyst.

The preferential formation of multi-carbon alcohols was further elaborated by density functional theory (DFT) calculations (Fig. 3b), investigating the adsorption energy of *CO with respect to Pd incorporated into the Cu moiety. Incorporating Pd onto the surface of the (100) facet of copper (Cu(100)) leads to decreased adsorption energies for *CO indifferent of the *CO coverage (Supplementary Fig. 13–15, Supplementary Tables 1 and 2). For example, pure Cu shows an adsorption energy of *CO (considering four *CO species) of −226 kJ mol^{-1} and gives more negative values with increasing Pd content. On the (100) facet of $Cu_{97}Pd_3$, adsorption of four CO molecules provides an adsorption energy of −251 kJ mol^{-1}, and further increasing the Pd content decreases the *CO adsorption energy to −354 kJ mol^{-1} on the (100) facet of $Cu_{75}Pd_{25}$ (Fig. 3b). The preferential *CO adsorption with increasing Pd content is consistent with the increased surface *CO concentration that would lead to a preference for C_{2+} product formation through the rate-determining OC*–*CO coupling step[27]. Similar trends in *CO adsorption energies were also observed for the (111) and stepped (211) facets upon Pd incorporation into the Cu phase (Supplementary Figs. 16 and 17 and Supplementary Tables 3 and 4). It should be noted that for a pure Pd phase, the *CO adsorption energy further decreases compared

https://doi.org/10.1038/s41560-023-01262-3

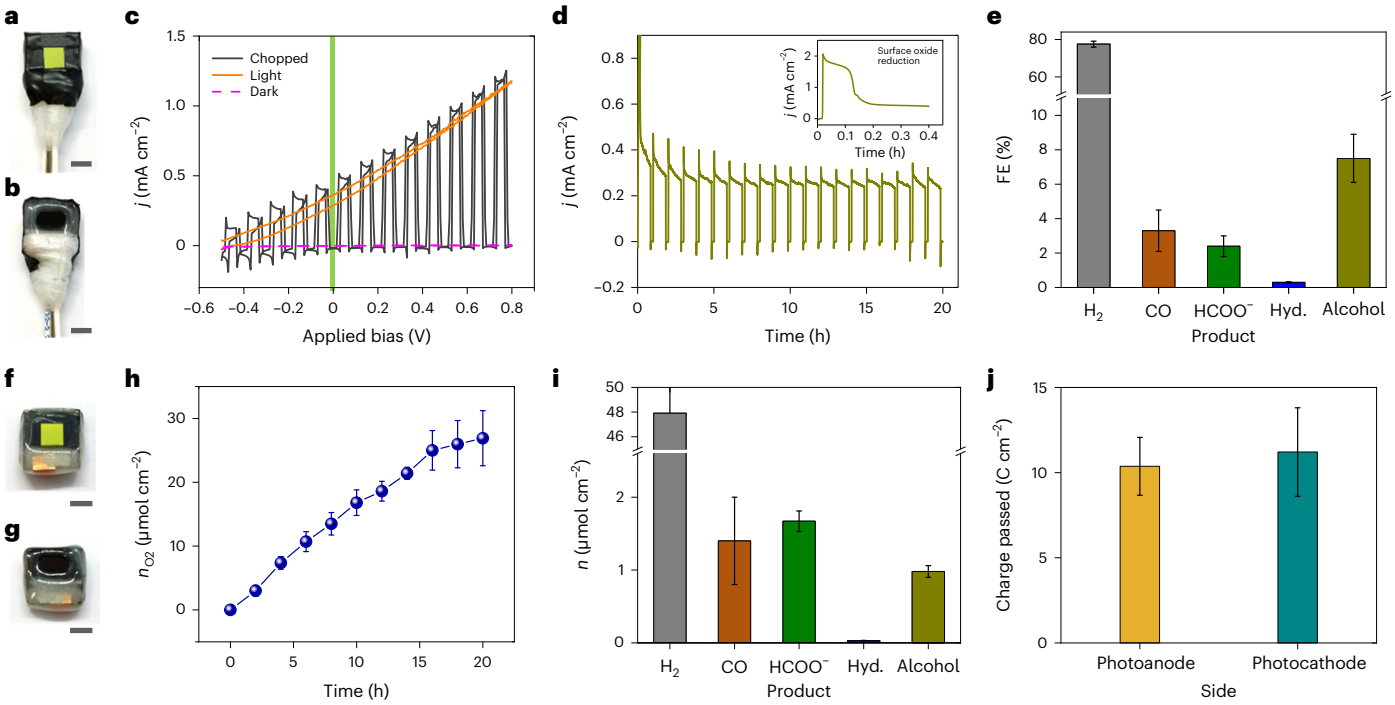

Fig. 4 | Unassisted multi-carbon alcohol production using wired tandem $BiVO_4$–perovskite|$Cu_{94}Pd_6$ devices and wireless standalone artificial leaves. a,**b**, Photographs of the wired tandem artificial leaf device showing the $BiVO_4$ side (**a**) and the $Cu_{94}Pd_6$ catalyst side (**b**). Scale bars, 5 mm. **c**, CV scans with the wired tandem device under chopped, continuous and no simulated solar-light illumination (AM 1.5 G; 100 mW cm^{-2}; scan rate, 10 mV s^{-1}), where the green vertical line indicates the photocurrent density (*j*) under no applied bias conditions. **d**, Representative transient for a 20 h bias-free CO_2 photoelectrolysis. Inset: the high initial photocurrent due to surface oxide reduction. **e**, FE of products from 20 h unassisted CO_2 photoelectrolysis. **f**,**g**, Photographs of the wireless standalone artificial leaf showing the $BiVO_4$ side (**f**) and the $Cu_{94}Pd_6$ catalyst side (**g**). Scale bars, 5 mm. **h**, Photoanodic O_2 quantification from the standalone artificial leaf, where n_{O2} denotes amount of oxygen produced. **i**, Amounts of products (*n*) formed at the photocathode from the standalone device after 20 h of light irradiation (1 sun, AM 1.5 G). **j**, Charge balance calculated from the products detected at the photocathode and photoanode sides of the standalone device after 20 h of operation. Hyd., total C_2 hydrocarbon. The *y*-axis breaks help to show the product distributions more clearly. The experiments were carried out at room temperature using CO_2-saturated aqueous 0.5 M $KHCO_3$ (pH 7.2). The mean values were estimated from three independent ($n = 3$) measurements, and the data are presented as mean values ± s.d.

with Cu or Cu_xPd_y (Supplementary Tables 1–3), where *CO is most likely bound too strongly and thereby acts as a poison for the Pd surface leading to diminished activity. Therefore the bimetallic electrocatalyst represents a more optimal *CO binding strength compared with the individual pure metals[41].

To further confirm the formation and stabilization of adsorbed *CO on the bimetallic surface, we performed operando Raman spectroscopy using the activated $Cu_{94}Pd_6$ catalyst at different applied potentials (Fig. 3c). The weak Cu_2O peaks (formed by aerial surface oxidation) at 521 and 624 cm^{-1} are observed at the open-circuit potential and disappear when applying a potential[23,42]. This observation supports that the active catalyst material is metallic without subsurface oxygen under the experimental cathodic conditions. The operando Raman spectra show expected features: $Cu_{94}Pd_6$–C stretching at 350 cm^{-1}, bicarbonate adsorption at around 1,080 cm^{-1}, HCOO* adsorption at 1,500 cm^{-1} and *C ≡ O stretching around 2,050 cm^{-1} (ref. 43). A key observation regarding the *CO adsorption on the activated $Cu_{94}Pd_6$ is the presence of *C ≡ O stretching at 0 V versus RHE. This finding indicates that the catalyst is active towards CO_2 reduction at very low overpotentials and a comparison with pure activated Cu shows the appearance of weak *C ≡ O stretching from −0.1 V versus RHE (Supplementary Fig. 18)[43]. The stabilized adsorbed *CO species facilitates the dimerization process and therefore the formation of multi-carbon products on the bimetallic catalyst surface. A shift in the wavenumber was observed when *C ≡ O stretching was compared under $^{13}CO_2$ and $^{12}CO_2$ atmosphere, which further supports the origin of the adsorbed intermediate is gaseous CO_2 (Supplementary Fig. 19). The *CO region shows a broad distribution of energies that can be explained by adsorption on different active sites[23,44] and by the sensitivity of the adsorption energy on Pd content, as discussed above. This strong *CO adsorption at low potentials thus supports the multi-carbon formation activity of the phase-separated $Cu_{94}Pd_6$ catalyst.

Unassisted solar multi-carbon alcohol production

An artificial leaf device assembly was finally constructed for solar multi-carbon alcohol generation from aqueous CO_2 and water (as the electron donor) using simulated solar irradiation. Caesium formamidinium methylammonium mixed-halide perovskite inverse-structure devices were interfaced with the activated $Cu_{94}Pd_6$ catalyst using a conductive graphite epoxy paste to obtain the photocathodes[15,23]. An additional PTAA hole transport layer[15] was introduced during the solar cell fabrication (Supplementary Fig. 20) to improve the open-circuit voltage (V_{oc}) compared to previously reported photoelectrodes (Methods; photovoltaic histograms and *J*–*V* curves are given in Supplementary Figs. 21 and 22)[13]. The graphite epoxy encapsulant provided improved long-term stability in aqueous medium and allowed us to integrate the catalyst directly to the perovskite layer to fabricate the perovskite|$Cu_{94}Pd_6$ photocathode. The photocathode was characterized by CV and CPE, where the experiments were carried out in a CO_2-saturated 0.5 M aqueous $KHCO_3$ solution (pH 7.2) under 1 sun solar irradiation (air mass (AM) 1.5 G, 100 mW cm^{-2}). A potential of +0.58 V versus RHE was applied on the photocathode during CPE studies as this is the overlap potential of the photocathode and the $BiVO_4$ photoanode

in a tandem assembly (Supplementary Fig. 23) and thus provides similar conditions as under unassisted tandem operation. After 6 h of the PEC experiment, a FE of (6.4 ± 0.9)% multi-carbon alcohol was obtained with an almost ~1:1 ethanol and *n*-propanol ratio (Supplementary Fig. 24).

To achieve solar-driven unassisted multi-carbon alcohol production coupled to water oxidation, tandem devices were assembled by connecting an O_2-evolving $BiVO_4$ photoanode (1 ± 0.1 μm thick, containing immobilized TiCo as an Earth-abundant, transparent, inexpensive and efficient water-oxidation catalyst; Supplementary Figs. 25 and 26) to the CO_2-reducing perovskite|$Cu_{94}Pd_6$ photocathode and illuminating with AM 1.5 G irradiation[22,23]. The artificial leaves were prepared in two ways: (1) a wired tandem device where both the photocathode and photoanode were connected to Cu wires so that the photocurrent transient could be measured with a potentiostat (Fig. 4a,b and Supplementary Fig. 27) and (2) a wireless standalone device where the photoanode and photocathode were directly connected by an integrated conductive copper tape (Fig. 4f,g and Supplementary Fig. 28). A CO_2-saturated aqueous 0.5 M $KHCO_3$ solution (pH 7.2) was used for the bias-free experiments as this reaction medium acts as a suitable buffer for both CO_2 conversion and O_2 evolution reactions and the $BiVO_4$ photoanode shows optimal operation and stability at neutral pH (refs. 22,45). The photocathode–photoanode overlap potential of +0.58 V versus RHE (Supplementary Fig. 23) and a bias voltage provided by the perovskite solar cell of 1.09 ± 0.01 V (Supplementary Fig. 21) should result in approximately −0.5 V versus RHE for the activated $Cu_{94}Pd_6$ catalyst under unassisted conditions. This potential falls within the optimal potential range (−0.47 V to −0.74 V versus RHE; Fig. 2a,b) for the multi-carbon alcohol production.

The CV of the wired tandem artificial leaf device revealed an onset at −0.4 V bias voltage, and a current density of ~300 μA cm^{-2} was observed at zero applied bias (Fig. 4c). PEC experiments under 20 h chopped irradiation (50 min on, 10 min off) were carried out with the wired tandem device under no applied bias, and a stable photocurrent was obtained to give 280 ± 30 μA cm^{-2} (Fig. 4d). A higher photocurrent density (~1.7 mA cm^{-2}) was initially obtained due to surface oxide reduction (inset, Fig. 4d) and after ~10 min, the photocurrent reached the steady-state value. The FE of multi-carbon alcohol reached a value of (7.5 ± 1.4)% after 20 h of PEC operation under 1 sun irradiation (Fig. 4e) where the individual FE of ethanol and *n*-propanol was (4.1 ± 0.6)% and (3.4 ± 0.8)%, respectively. Traces of C_2 hydrocarbons (ethylene and ethane; total FE = ~ 0.3%) were also produced along with H_2 (77.6 ± 1.6)%, CO (3.2 ± 1.2)% and $HCOO^-$ (2.4 ± 0.6)% formation. The calculated solar-to-fuel efficiency was ~0.31% where solar-to-alcohol efficiency was 0.025% (Supplementary Table 5). The FE of photoanodic O_2 was (79.2 ± 9.5)%, and this comparatively low FE_{O2} value could be attributed to the trapped O_2 bubbles and possibility of O_2 reduction at the photocathode. A PEC experiment with the tandem device under 20 h continuous light irradiation (no applied bias) provided similar product distribution as in the case of chopped light irradiation (Supplementary Fig. 29).

Standalone wireless artificial leaves operated under 1 sun irradiation, and the progress of the experiment was monitored by photoanodic O_2 quantification (Supplementary Video 1). Figure 4h shows a gradual increment of O_2 with time indicating that the leaf is functioning under light irradiation and around 26.9 ± 4.3 μmol cm^{-2} O_2 was obtained after 20 h irradiation. The amount of produced C_2, C_3 alcohols reached approximately 1 μmol cm^{-2} (0.58 ± 0.08 μmol cm^{-2} of ethanol and 0.40 ± 0.03 μmol cm^{-2} of *n*-propanol) after 20 h of operation (Fig. 4i). Under 1 sun irradiation, the rate of alcohol production amounted to ~40 μmol h^{-1} $g_{Cu94Pd6}{}^{-1}$. The time-dependent product distribution shows a gradual increase of liquid multi-carbon alcohol with time (Supplementary Fig. 30) that indicates the standalone artificial leaf performs steadily for a long time without degradation. The number of charges associated to form different products at the photoanode and photocathode were calculated from the amounts of products, and an even charge balance (Fig. 4j) between the photocathode and the photoanode has been obtained.

The product formation rate and solar-to-fuel efficiency of the artificial leaf device can be further improved by optimizing the perovskite and $BiVO_4$ light absorbers to obtain better overlap potentials, developing efficient catalyst systems that can suppress the hydrogen evolution reaction and produce multi-carbon alcohols more selectively, using a less energy-demanding oxidation process (such as plastic or biomass oxidation)[46,47] or employing a gas-diffusion photocathode assembly under continuous-flow reaction conditions[48].

Post-catalysis characterization of the activated bimetallic catalyst revealed only minor chemical and morphological changes after the unassisted PEC experiments. Post-experiment SEM and TEM analysis shows that some agglomeration occurred on the dendritic nanostructures (Supplementary Figs. 3 and 5), whereas post-experiment HAADF-STEM-EDX mapping showed the presence of separated Cu-rich and Pd-rich phases (Supplementary Fig. 6) with almost unchanged compositions. The overall metal composition was intact as the post-experiment ICP-OES study provided a Cu and Pd ratio close to 94:6 (Supplementary Fig. 2). Post-experiment XPS analysis shows the presence of Pd and Cu on the surface without any contamination (Supplementary Fig. 9). These analyses support a robust activated $Cu_{94}Pd_6$ material performing solar-driven multi-carbon alcohol production from aqueous CO_2 for extended periods of time.

Conclusions

We demonstrate a standalone artificial leaf device that produces multi-carbon alcohols directly from aqueous CO_2 and water under 1 sun irradiation. An activated $Cu_{94}Pd_6$ bimetallic catalyst is interfaced with a bias-free perovskite-$BiVO_4$ tandem device for solar-driven multi-carbon ($C_{2,3}$) product formation. The phase-separated bimetallic material is electrocatalytically active towards multi-carbon generation at a low overpotential. DFT calculations reveal that the presence of Pd in the Cu moiety improves the *CO adsorption and stabilization, whereas the operando Raman study shows a strong *CO adsorption peak even at 0 V versus RHE, indicating the activated catalyst is suitable for multi-carbon alcohol production at very low overpotentials. The wired $Cu_{94}Pd_6$ | perovskite–$BiVO_4$ tandem artificial leaf device shows a reasonable steady-state photocurrent of 280 ± 30 μA cm^{-2} and produces 7.5% FE for multi-carbon alcohols under 1 sun irradiation, whereas the wireless standalone artificial leaf produces ~1 μmol cm^{-2} multi-carbon alcohols after 20 h of operation with a production rate of ~40 μmol h^{-1} $g_{Cu94Pd6}{}^{-1}$. This proof-of-concept can be applied to form different long-chain complex fuels and chemicals by developing novel artificial leaf systems.

Methods

Materials and chemicals

Copper foil (99.9%), graphite foil (99.9%) and platinum foil (99.99%) were purchased from Alfa Aesar; orthophosphoric acid (68%) was purchased from Fluka. Copper(II) sulfate pentahydrate ($CuSO_4 \cdot 5H_2O$, 99.995%), sodium tetrachloropalladate (Na_2PdCl_4, 98%) and suprapur sulfuric acid (H_2SO_4, 96%) were purchased from Merck. Ethylene glycol (99%), sodium fluoride (NaF, 99.99%), potassium hydroxide (KOH, 99.999%) and sodium hydroxide (NaOH, 99.999%) were purchased from Merck. Polytetrafluoroethylene (PTFE) tape was purchased from Arctic Buffalo. Conductive fluorine-doped tin oxide (FTO) glass substrate (~7Ω per square), anhydrous *N*,*N*-dimethyl formamide (DMF, 99.8%), nickel nitrate hexahydrate ($Ni(NO_3)_2 \cdot 6H_2O$, ≥ 98.5%), polyethylenimine (PEIE, 80% ethoxylated solution, 35–40 wt% in H_2O, average molecular weight (M_w) 70,000), 2,3,5,6-Tetrafluoro-7,7,8,8-tetracyanoquinodimethane (F4TCNQ, 97%), H_2O_2 solution (30%), poly(triarylamine) (PTAA) and graphite powder were purchased from Sigma Aldrich. 1-methyl-2-pyrrolidone (NMP, 99.5%, extra dry over molecular sieves), ethylene glycol (99.8%, anhydrous), chloroform (99.9%, extra dry over molecular sieves), Zn dust (98 + %) and

chlorobenzene (≥99.5%, extra dry over molecular sieves), were bought from ACROS. Perovskite precursors lead iodide (PbI_2, 99.99%,) and lead bromide ($PbBr_2$, 99.99%) were purchased from TCI. Ethylenediamine (absolute, ≥99.5%) and hydrochloric acid (reagent grade) were purchased from Fluka. Formamidinium iodide and methylammonium bromide were purchased from Dyesol and dimethyl sulfoxide (DMSO, ACS reagent, ≥99.9% and 99 + %) from Alfa Aesar. Analytical reagent-grade chloroform, NaI (laboratory reagent grade) and acetonitrile (HPLC grade) were purchased from Fischer Scientific. (6,6)-phenyl C_{61} butyric acid methyl ester (PCBM, 99%) was bought from Solenne BV and isopropyl alcohol (2-propanol, ≥99.5%) from Honeywell. Bismuth nitrate pentahydrate ($Bi(NO_3)_3 \cdot 5H_2O$, 98%) was purchased from Sigma Aldrich, vanadyl acetyl acetonate $VO(acac)_2$, ≥97.0%) was purchased from Fluka and sodium hydroxide (NaOH, analytical reagent grade) was purchased from Fisher Scientific. ACS reagent-grade $KHCO_3$ (≥ 99.7%) was bought from Sigma Aldrich. CO_2 (CP grade, 99.995%) was received from BOC and $^{13}CO_2$ (99.0 atom% ^{13}C) was purchased from Sigma Aldrich. Methyl viologen dichloride ($MVCl_2$) and sodium sulfate Na_2SO_4 (99.9%) were purchased from Sigma Aldrich.

Milli-Q water (4 parts per billion of total organic carbon content, 18.2 MΩ cm) was used to prepare the electrolytes. All chemicals were used as purchased without further purification.

Synthesis of the catalyst

The Cu_xPd_y catalysts were synthesized via a dynamic hydrogen bubble template-assisted electrodeposition method following previously reported protocols[23,36]. The bimetallic alloy material was electrodeposited on a Cu foil substrate. Before electrodeposition, the substrates were electropolished in 50% orthophosphoric acid by applying +2.0 V against a graphite foil counter electrode for 90 s to remove any contamination from the Cu foil surface. The active area of the substrate was fixed by masking the excess substrate area by inert PTFE tape.

The electrodeposition was performed in a glass beaker containing copper sulfate and sodium tetrachloropalladate precursor salts (0.05 M total concentration of salts) in 1.5 M sulfuric acid solution[36]. Different compositions of the bimetallic material were achieved by changing the precursor salt ratio in the deposition bath. A three-electrode set-up was used for electrodeposition of the bimetallic Cu_xPd_y materials, where the electropolished Cu foil substrate was used as a working electrode, a Pt foil (2.5 × 2.5 cm) as the counter electrode and a leakless Ag/AgCl (saturated NaCl, BASi) electrode as the reference electrode. A current density of $j = -3.0$ A cm^{-2} was applied for 40 s for the galvanostatic electrodeposition process where vigorous H_2 bubbles were produced on the working electrode and acted as a template to form macroporous foam structure of the material. After preparation, the catalysts were dipped in Milli-Q water for 150 s and dried under gentle N_2 stream at room temperature.

Activation of the catalyst

After preparation, the as-prepared materials were activated to obtain the phase-separated oxide-derived catalyst to produce multi-carbon alcohols. A step-by-step multi-activation procedure was used. First, an oxide layer was formed by electrochemical anodization where +10 V was applied against a Pt foil cathode (2 cm × 2 cm) for 120 s. The electrolyte for anodization contained 0.15 M NaOH and 0.08 M NaF in a mixture of ethylene glycol and water (3:1 v/v ratio, pH ~12) (ref. 49). After anodization, the catalyst was then kept in Milli-Q water for 20 min with occasional shaking to remove any hydroxide (pale blue) precipitate and then dried overnight at room temperature in air. Then, the bimetallic catalyst was further annealed at 200 °C in air for 3 h to form a thick oxide layer. Finally, the oxide layer was electrochemically reduced to metallic phase by applying −0.6 V versus RHE for 30 min in a CO_2-saturated 0.5 M $KHCO_3$ electrolyte (pH 7.2). Reduction of the thick oxide layer forms dense nanocrystals on the dendrites with high electrochemically active surface area. The oxide-derived catalyst was then rinsed with Milli-Q water and dried under N_2. A surface oxide layer formed again due to aerial oxidation when the activated catalyst was exposed in air during the artificial leaf assembly. However, the oxide layer was quickly reduced back to metallic phase under the experimental conditions (Fig. 4d). The catalyst loading was determined by gravimetric analysis.

Inverse-structure perovskite device fabrication

Inverse-structure triple-cation mixed-halide perovskite photovoltaic cells were prepared following a previously reported method[15]. First, the active area (~0.5 cm × 0.5 cm) on the FTO substrate was fixed by etching away excess FTO with Zn dust and HCl. A NiO_x hole transport layer was deposited on the FTO-coated glass by spin coating a 1.0 M $Ni(NO_3)_2 \cdot 6H_2O$, 1.0 M ethylenediamine solution in ethylene glycol followed by a thermal annealing step at 573 K. A second hole transport layer PTAA doped with F4TCNQ was then spin coated on top of NiO_x under N_2 atmosphere. A caesium formamidinium methylammonium (CsFAMA) perovskite precursor solution was prepared following a stepwise method. A $FAMA_{0.22}Pb_{1.32}I_{3.2}Br_{0.66}$ solution (total 1,000 µl) was prepared with 510 µl of DMF, 340 µl of DMSO and 150 µl of NMP and then 48 µl of 1.5 M CsI in DMSO were added. The perovskite solution was next deposited onto the PTAA layer by spin coating in two steps: first 10 s at 1,000 rpm speed and then 35 s at 6,000 rpm speed using chloroform as the antisolvent added ~7 s before the end of spin coating. The perovskite layer was then annealed at 373 K for 30 min forming a dark film on top of the FTO substrate. Afterwards, a thin (6,6)-phenyl C_{61} butyric acid methyl ester (PCBM) electron transport layer (ETL) was deposited on top of the perovskite layer by spin coating 35 mg ml^{-1} PCBM solution in chlorobenzene for 45 s at 3,000 rpm. To prevent interfacial degradation, a PEIE film was further deposited on the PCBM layer by spin coating 3.87 µl ml^{-1} PEIE solution in IPA at 3,000 rpm for 30 s. A 100 nm silver layer was deposited by metal evaporation as an electrical contact. All the perovskite photovoltaic cells used in this study had active areas between 0.20 to 0.25 cm^2.

Preparation of the $BiVO_4$|TiCo photoanode

A reported procedure was followed to prepare the $BiVO_4$ photoanodes[50]. First, electrodeposition of a BiOI film was carried out onto an FTO-coated glass substrate (with an active area ~0.5 × 0.5 cm^2) from a precursor solution containing 20 ml of an aqueous $Bi(NO_3)_3 \cdot 5H_2O$ (0.02 M), NaI (0.4 M) solution and a 0.3 M benzoquinone solution in ethanol (9 ml). The potentiostatic electrodeposition was carried out by applying two different bias regimes: (1) −0.3 V versus Ag/AgCl for 5 s and then (2) −0.1 V versus Ag/AgCl for 180 s. Then, 40 µl cm^{-2} of a vanadium precursor solution (0.4 M $VO(acac)_2$, acac = acetyl acetonate) was drop casted onto the electrodeposited BiOI, followed by annealing at 723 K for 1 h to form the $BiVO_4$ photoanodes. The $BiVO_4$ samples were washed with aqueous NaOH (0.2 M) to dissolve excess V_2O_5 from the surface. Finally, an amorphous water-oxidation catalyst layer was deposited on the $BiVO_4$ surface by spin coating 20 µl cm^{-2} of a ($Ti_4O(OEt)_{15}(CoCl)$) precursor solution (4.8 mg ml^{-1}, in dry toluene) at 2,000 rpm for 10 s under air to form the active $BiVO_4$|TiCo photoanode[13,23].

Preparation of perovskite|$Cu_{94}Pd_6$ photocathodes

A conductive epoxy paste was used to interface the catalyst with the perovskite photoabsorber. The paste was prepared by homogeneously mixing graphite powder with Araldite standard two-component epoxy (3:4 mass ratio)[15,23]. The activated $Cu_{94}Pd_6$ catalyst was integrated to the device with the help of a thin layer of the conductive paste and then the device was kept overnight in air for drying. Finally, the exposed device edges were encapsulated by an Araldite 5 min rapid epoxy layer.

Assembly of the wired tandem artificial leaf device

The excess area of the $BiVO_4$ photoanode was also encapsulated by the Araldite 5 min rapid epoxy layer after attaching a connecting Cu wire to the FTO-coated glass with conductive Ag paste. For a wired tandem

assembly, the perovskite|$Cu_{94}Pd_6$ photocathode (contains a Cu wire connected to the FTO-coated glass for electrical contact) and the $BiVO_4$ photoanode were attached back to back by rapid epoxy glue[23]. The edges of the device were thoroughly encapsulated by the epoxy and kept overnight for drying. The inactive area of the $BiVO_4$|TiCo photoanode was covered by black tape to avoid direct perovskite irradiation through the bare glass substrate.

Assembly of the wireless standalone artificial leaf

A stepwise assembly process is required to make the standalone artificial leaf device. At first, the edges of the perovskite|$Cu_{94}Pd_6$ photocathode and the $BiVO_4$|TiCo photoanode were encapsulated by the Araldite 5 min rapid epoxy layer. Then these two devices were attached to each other by epoxy. A conductive Cu tape was used to connect the photocathode and the photoanode and then all the edges of the integrated device were encapsulated by the rapid epoxy and kept overnight for drying[22]. The standalone device was attached to a metal rod using Parafilm for physical support during operation. The inactive area of the photoanode was also covered by a black tape.

Electrochemical and PEC measurements

A certified Newport 1916-R optical power meter was used to calibrate a Newport Oriel 67005 solar light simulator with air mass 1.5 global (AM 1.5 G) solar filters to 100 mW cm^{-2} (1 sun) before each PEC experiment. All electrochemical and PEC experiments were conducted with a PalmSens Multi EmStat^{3+} and Ivium CompactStat potentiostats. The reaction medium for the experiments was an aqueous 0.5 M $KHCO_3$ buffer solution, which was purged for at least 30 min before the experiments with gaseous CO_2 containing 2% CH_4 as an internal standard to monitor any gas leakage in our reactors. Experiments under pure CO_2 and CO_2 with 2% CH_4 indicate no influence of CH_4 on the catalytic processes (Supplementary Fig. 31); therefore, it can be considered as an inert internal standard. The three-electrode set-up consisted of a Ag/AgCl (saturated NaCl) (BasiMW-2030) reference, a platinum mesh counter and a Cu_xPd_y or a perovskite|Cu_xPd_y working electrode in a two-compartment gas tight cell. PEC measurements were performed under chopped light irradiation (50 min on, 10 min off). All the experiments were carried out at room temperature. A Nafion^{117} (Fuel Cell Stores) proton exchange membrane was used to separate the cathode and anode compartments. All potentials measured with respect to the Ag/AgCl reference were converted to the reversible hydrogen scale using the equation:

$$E\,(\text{V versus RHE}) = E\,(\text{V versus Ag/AgCl}) + 0.059\,\text{V} \times \text{pH} + 0.197\,\text{V at 298 K}.$$

The bias-free solar-driven experiments were carried out using a wired tandem artificial leaf device or a wireless standalone artificial leaf assembled in a back-to-back configuration in a one-compartment cell using CO_2 saturated aqueous 0.5 M $KHCO_3$ (pH 7.2) at room temperature.

Product analysis

The photoanodic O_2 evolution was monitored by a NeoFox-GT and Fospor-R fluorescence oxygen sensor probe from Ocean Optics. CO and H_2 from the Cu_xPd_y cathode and perovskite|Cu_xPd_y photocathode were quantified by manual injection from the headspace of the reactors into a Shimadzu GC-2010 Plus gas chromatograph. C_2 hydrocarbons from the headspace and C_2 and C_3 alcohols from the electrolyte were quantified using an Agilent 7890 A gas chromatograph equipped with a flame ionization detector and a thermal conductivity detector. A combination of a PLOT-MS 5 A Molsieve column and a PLOT-Q column was used for hydrocarbon separation, and a HP5 column was used for alcohol separation. Two separate injectors were used for gaseous and liquid product injection. A glass wool containing pre-column before the HP5 column prevented the electrolyte salt ($KHCO_3$) from entering the column. The pre-column was replaced time to time to avoid any obstacles in the gas flow due to salt accumulation. The temperature of the liquid injector was kept at 210 °C to instantly transfer the liquid aliquot into the gas phase. In addition, the HP5 (alcohol separating column) was opened time to time and re-plumbed carefully after cutting an initial portion to avoid contamination from salts and dust. After experiment, the electrolyte solution was also analysed by ion exchange chromatography (Metrohm 882 IC Plus) to quantify formate. The FEs of the products were calculated using the following equation: $FE_{product}(\%) = (nzF/Q_{passed}) \times 100$, where n is the number of moles of product formed, z is the number of electrons involved to generate that product, F is the Faraday constant and Q_{passed} is the total amount of charge passed during the experiment. The number of electrons involved to form ethanol is 12, n-propanol is 18, ethylene is 12, ethane is 14, carbon monoxide is 2, formate is 2, hydrogen is 2 and oxygen is 4. The liquid aliquot after the isotopic labelling experiments was analysed by ^1H NMR spectroscopy (Bruker 500 MHz, using D_2O solvent) to distinguish between unlabelled ^{12}C and labelled ^{13}C products. The reaction medium for the isotopic labelling experiment was prepared by purging $^{13}CO_2$ (99 atom%) into ultrapure 0.5 M KOH (99.999%) solution. Some natural abundance (~1%) of $^{12}CO_2$ in the $^{13}CO_2$ cylinder results the appearance of small peaks of unlabelled products in the ^1H NMR analysis.

Operando Raman spectroscopy

Measurements were recorded on a Renishaw inVia microscope coupled to a 785 nm laser with typical power of 0.42 mW through a 20× objective with 30 s typical integration time. A specially designed three-electrode cell with a platinum mesh (Alfa Aesar) counter electrode, a Ag/AgCl (3.0 M KCl, eDAQ ET072, Green Leaf Scientific) reference electrode and an activated Cu_xPd_y working electrode has been used. $^{12/13}CO_2$-saturated 0.5 M aqueous $KH^{12/13}CO_3$ solutions (pH 7.2) were used, and the experiments were carried out at room temperature. The cell is closed by a 25 mm × 25 mm × 0.2 mm glass cover slip. Electrochemical measurements were recorded at room temperature on an Autolab PGSTAT204 (Metrohm).

Computational details

All DFT calculations were performed on the Quantum Espresso 6.4 code using the projector augmented wave method and pseudopotentials with plane wave and density cut-offs of 40 Rydberg (Ry) and 200 Ry, respectively, with a Fermi-level smearing of 0.01 Ry using the revised PBE exchange functional. The optimizations converged if the forces were below 0.001 Ry $Bohr^{-1}$. Cu slab models were constructed from optimized bulk Cu (lattice constant 3.65 Å) using an 11 × 11 × 11 Monkhorst–Pack k-point grid. A bulk Cu_3Pd_1 face-centred cubic metal alloy was constructed and optimized using an 11 × 11 × 11 Monkhorst–Pack k-point grid to generate the $Cu_{75}Pd_{25}$ slab models. Molecular CO was calculated in a 15 × 15 × 15 Å cubic unit cell using a 1 × 1 × 1 Monkhorst–Pack k-point grid.

Cu(111) and Cu(100) slabs consisted of four layers with 9 and 8 Cu atoms, respectively, per layer with the bottom two layers kept frozen and a 4 × 4 × 1 Monkhorst–Pack k-point grid. Cu(211) slabs were constructed in a 3 × 4 cell with 32 Cu atoms and four copper layers along the Cu(111) direction with the bottom layer (12 Cu atoms) kept frozen and a 4 × 4 × 1 Monkhorst–Pack k-point grid. The slab models along the (111), (100) and (211) facets for $Cu_{75}Pd_{25}$ were constructed the same way. For $Cu_{97}Pd_3$, one surface Cu atom was replaced by one Pd atom on the Cu(111) and Cu(100) slabs. In the case of Cu(211), two models were constructed with either one copper at the top layer (denoted $Cu_{97}Pd_3$(211)_1) or the second top layer (denoted $Cu_{97}Pd_3$(211)_2) was replaced by one palladium atom. Larger (211) slab models of Cu and $Cu_{97}Pd_3$ were constructed with a 6 × 4 cell with 64 atoms to benchmark the effect of the slab size on the CO adsorption energies on (211) facets, which did not show any difference indifferent of the slab size. All the slab models had a vacuum layer of 20 Å.

The adsorption energy of CO was calculated based on the difference in electronic energy between the CO-coordinated slab, and the slab and CO in the gas phase: $E_{Ads-CO} = E_{Slab-CO} - E_{Slab} - E_{CO}$, where E_{Ads-CO} is the adsorption energy, $E_{Slab-CO}$ the electronic energy of the CO-coordinated slab, E_{Slab} the electronic energy of the slab and E_{CO} the electronic energy of CO in vacuum.

Material characterization

A TESCAN MIRA3 field emission gun-scanning electron microscope equipped with an Oxford Instruments Aztec Energy X-maxN 80 EDX system was used for the SEM and EDX analyses. The TEM images, HAADF-STEM images and EDX maps were collected using a Thermo Scientific Talos F200X G2 TEM operating at 200 kV. TEM images were recorded using a 16M complementary metal oxide–semiconductor camera. STEM images were collected using a Fischione HAADF detector at a camera length of 98 mm and EDX maps using a Super-X detector system. Holey carbon film on 300 mesh Ni grids and a low-background beryllium double tilt sample holder were used. XPS analyses were performed at the Maxwell Center (University of Cambridge) with a near ambient pressure X-ray photoemission spectroscopy system that uses a SPECS XR 50 MF X-ray Source, μ-FOCUS 600 X-ray monochromator and differentially pumped PHOIBOS 150 1D-DLD near ambient pressure analyser. Data analyses were carried out using CasaXPS software. A Gaussian/Lorentzian line shape was used for fitting. The fit details for the activated $Cu_{94}Pd_6$ catalyst (Fig. 1f,g and Supplementary Fig. 9b,c) are: Cu $2p_{3/2}$ peak position 931.66 eV with area% 71.4, Cu $2p_{1/2}$ peak position 951.5 eV with area% 28.6, Pd $3d_{5/2}$ peak position 334.57 eV with area% 60.3 and Pd $3d_{3/2}$ peak position 339.89 eV with area% 39.7. The fit details for post-experiment activated $Cu_{94}Pd_6$ catalyst (Supplementary Fig. 9e,f) are: Cu $2p_{3/2}$ peak position 931.7 eV with area% 71.7, Cu $2p_{1/2}$ peak position 951.53 eV with area% 28.3, Pd $3d_{5/2}$ peak position 334.52 eV with area% 60.8 and Pd $3d_{3/2}$ peak position 339.85 eV with area% 39.2. Powder XRD measurements were performed by a Panalytical X'Pert Pro (K alpha Cu radiation) diffractometer using 1° min^{-1} scan rate. ICP-OES measurements were performed using a Thermo Scientific iCAP 7400 ICP-OES DUO spectrometer.

Data availability

The raw data supporting the findings of this study are available from the University of Cambridge data repository: https://doi.org/10.17863/CAM.95679.

References

1. Concepcion, J. J., House, R. L., Papanikolas, J. M. & Meyer, T. J. Chemical approaches to artificial photosynthesis. *Proc. Natl Acad. Sci. USA* **109**, 15560–15564 (2012).
2. Hammarström, L. & Hammes-Schiffer, S. Artificial photosynthesis and solar fuels. *Acc. Chem. Res.* **42**, 1859–1860 (2009).
3. Benson, E. E., Kubiak, C. P., Sathrum, A. J. & Smieja, J. M. Electrocatalytic and homogeneous approaches to conversion of CO_2 to liquid fuels. *Chem. Soc. Rev.* **38**, 89–99 (2009).
4. Zhuang, T.-T. et al. Copper nanocavities confine intermediates for efficient electrosynthesis of C_3 alcohol fuels from carbon monoxide. *Nat. Catal.* **1**, 946–951 (2018).
5. Rahaman, M., Dutta, A., Zanetti, A. & Broekmann, P. Electrochemical reduction of CO_2 into multicarbon alcohols on activated Cu mesh catalysts: an identical location (IL) study. *ACS Catal.* **7**, 7946–7956 (2017).
6. Zhuang, T.-T. et al. Steering post-C–C coupling selectivity enables high efficiency electroreduction of carbon dioxide to multi-carbon alcohols. *Nat. Catal.* **1**, 421–428 (2018).
7. Ji, L. et al. Highly selective electrochemical reduction of CO_2 to alcohols on an FeP nanoarray. *Angew. Chem. Int. Ed.* **59**, 758–762 (2020).
8. Gu, Z. et al. Efficient electrocatalytic CO_2 reduction to C_{2+} alcohols at defect-site-rich Cu surface. *Joule* **5**, 429–440 (2021).
9. Wang, Z. et al. Efficient ambient-air-stable solar cells with 2D–3D heterostructured butylammonium-caesium-formamidinium lead halide perovskites. *Nat. Energy* **2**, 17135 (2017).
10. Swarnkar, A. et al. Quantum dot induced phase stabilization of α-$CsPbI_3$ perovskite for high-efficiency photovoltaics. *Science* **354**, 92–95 (2016).
11. Wang, Z. et al. High irradiance performance of metal–halide perovskites for concentrator photovoltaics. *Nat. Energy* **3**, 855–861 (2018).
12. Snaith, H. J. Present status and future prospects of perovskite photovoltaics. *Nat. Mater.* **17**, 372–376 (2018).
13. Andrei, V. et al. Scalable triple-cation mixed-halide perovskite–$BiVO_4$ tandems for bias-free water splitting. *Adv. Energy Mater.* **8**, 1801403 (2018).
14. Zhang, H. et al. A sandwich-like organolead halide perovskite photocathode for efficient and durable photoelectrochemical hydrogen evolution in water. *Adv. Energy Mater.* **8**, 1800795 (2018).
15. Pornrungroj, C. et al. Bifunctional perovskite–$BiVO_4$ tandem devices for uninterrupted solar and electrocatalytic water splitting cycles. *Adv. Funct. Mater.* **31**, 2008182 (2021).
16. Schreier, M. et al. Efficient photosynthesis of carbon monoxide from CO_2 using perovskite photovoltaics. *Nat. Commun.* **6**, 7326 (2015).
17. Gao, J. et al. Solar water splitting with perovskite/silicon tandem cell and TiC-supported Pt nanocluster electrocatalyst. *Joule* **3**, 2930–2941 (2019).
18. Luo, J. et al. Water photolysis at 12.3% efficiency via perovskite photovoltaics and Earth-abundant catalysts. *Science* **345**, 1593–1596 (2014).
19. Zhang, H. et al. Carbon encapsulation of organic–inorganic hybrid perovskite toward efficient and stable photo-electrochemical carbon dioxide reduction. *Adv. Energy Mater.* **10**, 2002105 (2020).
20. Bhattacharjee, S. et al. Reforming of soluble biomass- and plastic-derived waste using a bias-free $Cu_{30}Pd_{70}$|perovskite|Pt photoelectrochemical device. *Adv. Funct. Mater.* **32**, 2109313 (2022).
21. Chen, J. et al. Compositionally screened eutectic catalytic coatings on halide perovskite photocathodes for photoassisted selective CO_2 reduction. *ACS Energy Lett.* **4**, 1279–1286 (2019).
22. Andrei, V., Reuillard, B. & Reisner, E. Bias-free solar syngas production by integrating a molecular cobalt catalyst with perovskite–$BiVO_4$ tandems. *Nat. Mater.* **19**, 189–194 (2020).
23. Rahaman, M. et al. Selective CO production from aqueous CO_2 using a $Cu_{96}In_4$ catalyst and its integration into a bias-free solar perovskite–$BiVO_4$ tandem device. *Energy Environ. Sci.* **13**, 3536–3543 (2020).
24. Huan, T. N. et al. Low-cost high-efficiency system for solar-driven conversion of CO_2 to hydrocarbons. *Proc. Natl Acad. Sci. USA* **116**, 9735–9740 (2019).
25. Gurudayal et al. Efficient solar-driven electrochemical CO_2 reduction to hydrocarbons and oxygenates. *Energy Environ. Sci.* **10**, 2222–2230 (2017).
26. Roh, I. et al. Photoelectrochemical CO_2 reduction toward multicarbon products with silicon nanowire photocathodes interfaced with copper nanoparticles. *J. Am. Chem. Soc.* **144**, 8002–8006 (2022).
27. Nitopi, S. et al. Progress and perspectives of electrochemical CO_2 reduction on copper in aqueous electrolyte. *Chem. Rev.* **119**, 7610–7672 (2019).
28. Yu, J. et al. Recent progresses in electrochemical carbon dioxide reduction on copper-based catalysts toward multicarbon products. *Adv. Funct. Mater.* **31**, 2102151 (2021).

29. Edwardes Moore, E. et al. A semi-artificial photoelectrochemical tandem leaf with a CO_2-to-formate efficiency approaching 1%. *Angew. Chem. Int. Ed.* **60**, 26303–26307 (2021).
30. Kuhl, K. P., Cave, E. R., Abram, D. N. & Jaramillo, T. F. New insights into the electrochemical reduction of carbon dioxide on metallic copper surfaces. *Energy Environ. Sci.* **5**, 7050–7059 (2012).
31. Hori, Y., Wakebe, H., Tsukamoto, T. & Koga, O. Electrocatalytic process of CO selectivity in electrochemical reduction of CO_2 at metal electrodes in aqueous media. *Electrochim. Acta* **39**, 1833–1839 (1994).
32. Dickinson, H. L. A. & Symes, M. D. Recent progress in CO_2 reduction using bimetallic electrodes containing copper. *Electrochem. Commun.* **135**, 107212 (2022).
33. Li, Y. C. et al. Binding site diversity promotes CO_2 electroreduction to ethanol. *J. Am. Chem. Soc.* **141**, 8584–8591 (2019).
34. Ma, S. et al. Electroreduction of carbon dioxide to hydrocarbons using bimetallic Cu–Pd catalysts with different mixing patterns. *J. Am. Chem. Soc.* **139**, 47–50 (2017).
35. Lyu, Z. et al. Kinetically controlled synthesis of Pd–Cu janus nanocrystals with enriched surface structures and enhanced catalytic activities toward CO_2 reduction. *J. Am. Chem. Soc.* **143**, 149–162 (2021).
36. Rahaman, M. et al. Selective *n*-propanol formation from CO_2 over degradation-resistant activated PdCu alloy foam electrocatalysts. *Green Chem.* **22**, 6497–6509 (2020).
37. Li, J. et al. Enhanced multi-carbon alcohol electroproduction from CO via modulated hydrogen adsorption. *Nat. Commun.* **11**, 3685 (2020).
38. Gao, D. F. et al. Size-dependent electrocatalytic reduction of CO_2 over Pd nanoparticles. *J. Am. Chem. Soc.* **137**, 4288–4291 (2015).
39. Zheng, Y. et al. Understanding the roadmap for electrochemical reduction of CO_2 to multi-carbon oxygenates and hydrocarbons on copper-based catalysts. *J. Am. Chem. Soc.* **141**, 7646–7659 (2019).
40. Kortlever, R., Shen, J., Schouten, K. J. P., Calle-Vallejo, F. & Koper, M. T. M. Catalysts and reaction pathways for the electrochemical reduction of carbon dioxide. *J. Phys. Chem. Lett.* **6**, 4073–4082 (2015).
41. van Santen, R. A., Neurock, M. & Shetty, S. G. Reactivity theory of transition-metal surfaces: a Brønsted–Evans–Polanyi linear activation energy–free-energy analysis. *Chem. Rev.* **110**, 2005–2048 (2010).
42. Dutta, A. et al. CO_2 electrolysis—complementary operando XRD, XAS and Raman spectroscopy study on the stability of Cu_xO foam catalysts. *J. Catal.* **389**, 592–603 (2020).
43. Jiang, S., Klingan, K., Pasquini, C. & Dau, H. New aspects of operando Raman spectroscopy applied to electrochemical CO_2 reduction on Cu foams. *J. Chem. Phys.* **150**, 041718 (2019).
44. Gunathunge, C. M. et al. Spectroscopic observation of reversible surface reconstruction of copper electrodes under CO_2 reduction. *J. Phys. Chem. C* **121**, 12337–12344 (2017).
45. Toma, F. M. et al. Mechanistic insights into chemical and photochemical transformations of bismuth vanadate photoanodes. *Nat. Commun.* **7**, 12012 (2016).
46. Uekert, T., Pichler, C. M., Schubert, T. & Reisner, E. Solar-driven reforming of solid waste for a sustainable future. *Nat. Sustain.* **4**, 383–391 (2021).
47. Bhattacharjee, S. et al. Photoelectrochemical CO_2-to-fuel conversion with simultaneous plastic reforming. *Nat. Synth.* **2**, 182–192 (2023).
48. Nguyen, T. N. & Dinh, C.-T. Gas diffusion electrode design for electrochemical carbon dioxide reduction. *Chem. Soc. Rev.* **49**, 7488–7504 (2020).
49. Allam, N. K. & Grimes, C. A. Electrochemical fabrication of complex copper oxide nanoarchitectures via copper anodization in aqueous and non-aqueous electrolytes. *Mater. Lett.* **65**, 1949–1955 (2011).
50. Lu, H. et al. Single-source bismuth (transition metal) polyoxovanadate precursors for the scalable synthesis of doped $BiVO_4$ photoanodes. *Adv. Mater.* **30**, 1804033 (2018).

Acknowledgements

This work was supported by the European Commission with a Horizon 2020 Marie Skłodowska-Curie Individual European Fellowship (SolarFUEL, GAN 839763, M.R.), the Cambridge Trust (Vice-Chancellor's Award to V.A., Cambridge Thai Foundation Award to C.P., HRH Prince of Wales Commonwealth Scholarship to S.B.), the Winton Programme for the physics of sustainability and St John's College (Title A research fellowship to V.A.), the EPSRC (EP/L015978/1, EP/L027151/1, D.W., J.J.B., E.R.), the Swiss National Science Foundation (Early Postdoctoral Mobility fellowship P2EZP2-191791, E.L.) and the Austrian Science Fund (FWF, Schrödinger Fellowship J-4381, C.M.P). Access to the Cambridge XPS system, part of the Sir Henry Royce Institute-Cambridge equipment (EPSRC grant EP/P024947/1) and funding for TEM (EPSRC Underpinning Multi-User Equipment Call, EP/P030467/1) are gratefully acknowledged. We thank C. M. Fernández-Posada for assistance with the XPS and S. Kar and Y. Liu (University of Cambridge) for their valuable feedback on the paper.

Author contributions

M.R. and E.R. designed the project. M.R. developed the bimetallic catalyst, assembled the artificial leaf devices and performed all the (photo)electrochemical experiments. V.A. prepared and characterized the perovskite and $BiVO_4$ light absorbers and made the supplementary video. D.W. performed the operando Raman experiments. E.L. carried out the DFT calculations. C.P. assisted with oxygen analysis and schematic diagrams. S.B. and C.M.P. assisted with the catalyst characterization and analytics. H.F.G. helped with electron microscopy analyses. J.J.B provided insights in Raman measurements. M.R. and E.R. collectively wrote the paper with input from all co-authors. E.R. supervised the work.

Competing interests

The authors declare no competing interests.

Additional information

Supplementary information The online version contains supplementary material available at https://doi.org/10.1038/s41560-023-01262-3.

Correspondence and requests for materials should be addressed to Erwin Reisner.

Peer review information *Nature Energy* thanks Kazuhiro Takanabe and the other, anonymous, reviewer(s) for their contribution to the peer review of this work.